ELSEVIER

Contents lists available at ScienceDirect

Journal of Power Sources

journal homepage: www.elsevier.com/locate/jpowsour





Deconvolution of the electrochemical impedance of Na/NaCrO₂ cells with ester- and ether-based electrolytes

Changlong Chen^a, Hao Lin^b, Bingyu Liu^a, Leon Shaw^{a,*}

- a Department of Mechanical, Materials and Aerospace Engineering, Chicago, IL, United States
- ^b Department of Chemistry, Illinois Institute of Technology, Chicago, IL, United States

HIGHLIGHTS

- Deconvolution of cell impedance into individual interfacial kinetics.
- Electrolyte-dependent Na metal labeling and relaxation time analysis.
- Physically-motivated equivalent circuit model for Na-ion batteries.
- Determination of performance-limiting steps for Na-ion batteries.

ARTICLE INFO

Keywords: Na-ion batteries Electrochemical impedance spectroscopy Ester-based electrolyte Ether-based electrolyte NaCrO $_2$ cathode

ABSTRACT

Na-ion battery is regarded as the most promising battery chemistry for the post Li-ion battery generation. Unlike Li-ion batteries, Na-ion batteries, due to the intrinsic instabilities, are rarely studied using electrochemical impedance spectroscopy to inspect the electrode kinetics within. Here, we combine the electrolyte-dependent Na metal labeling and distribution function of relaxation time analysis to readily deconvolute the conventional Nyquist spectrum of Na/NaCrO₂ cells into individual electrode processes. Utilizing the corresponding equivalent circuit model with physical implications, the performance-limiting kinetics of Na/NaCrO₂ cells with the typical ester-based electrolyte, PC/FEC, and ether-based one, diglyme, are precisely identified. Given the sluggish interference generated at the Na metal counter electrode with PC/FEC electrolyte, proper ether-based electrolytes are recommended to be adopted in the future validation of potential materials for Na-ion battery studies.

1. Introduction

Electrochemical impedance spectroscopy (EIS) is a powerful technique in probing various processes in multiple electrochemical systems [1,2], such as energy storage [3] and conversion [4], corrosion [5,6], etc. Bearing its high precision and non-destructive nature, EIS is extensively used in studying Li-ion batteries (LIBs), the most advanced energy storage technologies, to characterize different physicochemical processes within [7,8]. Through appropriate combinations over cell configurations, testing conditions and analyzing approaches, the kinetic processes, such as charge transfer at an interface and ion diffusion in a media, can be rationally resolved, which provides essential information for identifying the performance-limiting steps in the given LIB systems. However, as a critical alternative to LIBs [9,10], Na-ion batteries (NIBs) are rarely investigated systematically using EIS in a comprehensive

manner where most NIB studies treat EIS as a supplementary technique and interpret the data simply relying on the complex nonlinear least square (CNLS) approximation over the obtained Nyquist plot with experience-based pre-settled equivalent circuit model (ECM) [11–15].

This contrast in utilizing EIS technique between LIB and NIB studies probably originates from the discrepancy in the working electrode consistency and the counter electrode stability in these two systems. In previous LIB studies, the separation of impedance contributions from cathode and anode are usually achieved using symmetrical cells [16–21]. By manipulating either internal or external parameters, like state of charge (SOC), cell components, testing temperature, etc., the corresponding impedance variations can be directly linked to the characteristic behavior of certain processes in the given scenario. The established physicochemical model is further applied, optimized, and extended in the following work. As for NIB systems, this classic

E-mail address: lshaw2@iit.edu (L. Shaw).

^{*} Corresponding author.

post-mortem method is largely limited by the lack of homogeneous working electrode and the instabilities of the Na metal counter electrode. Due to the less abundance in the high-quality commercial active materials, such as LiCoO₂, LiNi_xMn_yCo_{1-z-y}O₂, LiFePO₄, graphite for LIBs [16-18,20,22-27], most NIB studies still adopt the home-made active materials with little or no rigorous quality control. This situation leads to some inhomogeneity in the working electrode and the constructed symmetrical cell. Additionally, the disassembling and reassembling steps during the symmetrical cell preparation will easily alter the dimensions of the Na metal because of its weak mechanical properties [28], and may destroy the surface chemistry as well because the surface roughness of commonly used glass fiber (GF) separator is much higher than that of polypropylene-based one for LIBs. All these generated artifacts in symmetrical cells will be reflected as pseudo processes and mismatches between the impedance results of full cells and symmetrical cells [17,19,21], which can increase the difficulty in identifying various electrode processes using EIS analysis for NIBs.

Herein, a novel logic in deconvoluting the EIS spectra for NIB studies is proposed and verified in this work without applying the classic postmortem analysis. According to the previous findings from multiple characterizations, including in situ optical microscopy [29,30], X-ray photoelectron spectroscopy (XPS) with depth profiling [30-33], and cryo-transmission electron spectroscopy (TEM) [32], it is obvious that Na metal behaviors are quite distinct in different electrolyte systems. For example, the propylene carbonate/fluoroethylene carbonate (PC/FEC) electrolyte, a representative in the ester-based electrolytes for NIBs [34-36], tends to cause dendritic and porous Na deposition, and also form thick and nonuniform organic-rich (like ROCO2Na) solid electrolyte interphase (SEI) layer on the Na metal surface [29,35]. In contrast, the Na deposition in the diglyme electrolyte, a promising candidate in the ether-based electrolytes [30,33,36-38], is comparatively flat and dense, which could be attributed to the formation of stable and thin inorganic-rich (e.g. NaF and Na2O) SEI layer on the Na metal surface [30,37]. A simplified schematic for Na metal surfaces in these two typical electrolytes is presented in Fig. 1a. Inspired by these previous studies, we consider that the distinctive Na metal behaviors discovered in these two electrolytes could be utilized as a feature labeling the electrode processes from the Na metal anode, which helps separate its

impedance contributions from the EIS spectra. Regarding the choice of working electrode, $NaCrO_2$, a standard O3-type layered oxide cathode, is chosen in this work, mainly owing to its relatively low upper cutoff voltage (3.6 V) [11,39,40]. This minimizes the oxidation of the chosen electrolyte systems and thus avoids the formation of the cathode electrolyte interphase (CEI) layer at the working electrode side, further simplifying the electrode processes to be identified.

The strategy of this study is to unravel the characteristics of the electrode processes of the NaCrO $_2$ working electrode and Na metal counter electrode first via in-situ EIS measurements of Na/NaCrO $_2$ cells in typical ester- and ether-based electrolytes at different SOCs and testing temperatures. Then, the number of electrode processes and the corresponding impedance characteristics are confirmed and captured with the aid of distribution of relaxation time (DRT) analysis where subtle variations of Nyquist curves can be detected [41]. Through proper identification of the impedance behaviors revealed in DRT results, a physically motivated ECM is established. Finally, in the light of fairly-deconvoluted Nyquist plots, the activation energies of existing interfacial kinetics on the NaCrO $_2$ and Na metal electrodes are calculated following the Arrhenius equation. The performance-limiting steps in the Na/NaCrO $_2$ cells with selected ester- and ether-based electrolytes are determined here as well.

2. Experimental

2.1. Preparation of NaCrO2 electrode

NaCrO₂ powder was synthesized via a conventional solid-state reaction [39,40,42]. Briefly, Cr_2O_3 (\geq 98%, Sigma Aldrich) and Na_2CO_3 (\geq 99.5%, Sigma Aldrich) powders were first ball-milled using a SPEX mill in a mole ratio of 1:1.03 for 3 h. Then, the mixed powder was pelletized and calcinated using a tube furnace in the flowing Ar at 900 °C for 5 h. The resulting pellet was quickly transferred into an Ar-filled glovebox and further grinded with agate mortar and pestle. The morphology and crystal structure of the as-prepared NaCrO₂ powder were confirmed using field emission scanning electron microscopy (FESEM) (JSM-6701, JEOL) and X-ray diffraction (XRD) (D2 Phaser diffractometer, Bruker) (Fig. S1). The as-synthesized NaCrO₂ powder,

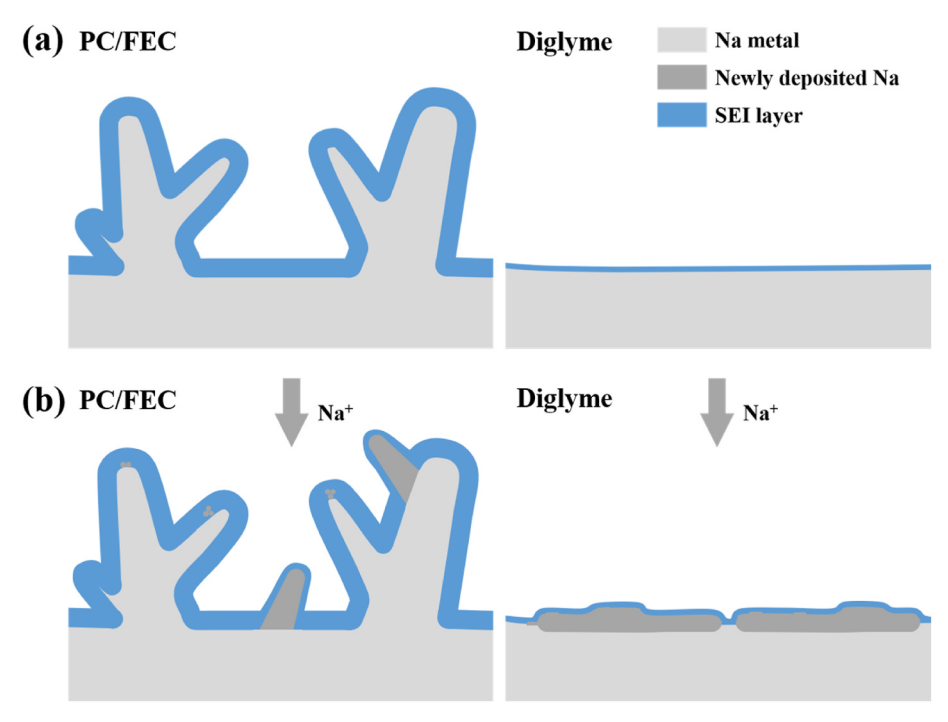


Fig. 1. Simplified schematics for (a) Na metal surfaces and (b) characteristic Na depositions in PC/FEC and diglyme electrolytes.

carbon black (CB), and polyvinylidene fluoride (PVDF) were mixed in a mass ratio of 8:1:1 with N-Methyl-2-pyrrolidone (NMP) solvent using a THINKY mixer to form a uniform slurry. Subsequently, the slurry was cast on an Al foil using a doctor blade with a spread gap of 150 μ m and dried in a vacuum oven at 60 °C for 6 h and 120 °C for 6 h to remove residual moisture. At last, 13-mm NaCrO₂ disc electrodes were punched and stored in the Ar-filled glovebox for the subsequent use. The mass loading of the active materials is \sim 1.8 mg/cm².

2.2. Electrochemical measurements

2032-type coin cells, comprising a NaCrO2 cathode, a home-made Na metal anode (\sim 14.3 mm in diameter and \sim 227 μ m in thickness, Table S1), and 2 GF/C separators (Whatman), were assembled with the addition of 130 µL electrolyte (1 M NaPF6 in PC:FEC (95:5 in vol) or diglyme solvents) where the electrolytes were pre-dried with 4 Å molecular sieves before usage. All the cells were first rest for 8 h and then cycled under C/10 current (1C = 125 mA/g) between 2 and 3.6 V with NEWARE battery testers for 3 cycles at room temperature (\sim 25 $^{\circ}$ C). Later, the cells were transferred into a temperature chamber (ESPEC) and further tested with the potentiostat (PARSTAT 4000A, AMETEK) in the frequency range from 10⁵ to 0.01 Hz. For the SOC-dependent EIS analysis, the EIS measurement was conducted every 10% SOC from 10 to 100% SOC during the charging process under C/10 current with the temperature fixed at 25 $^{\circ}\text{C}$. A 30- and 10-min rests were introduced before and after each EIS measurement respectively to achieve a relatively steady state for the measured cells. For the temperature dependent EIS analysis, the SOC of measured cells were fixed at 10% and the EIS measurement was conducted at 0, 10, 20, 30, 40 °C in sequence. To reach a stable status, the cells were soaked in the specified temperature for 45 min before the EIS measurement. The steady states of the measured cells were confirmed by a small voltage variation (<10 mV) before and after each EIS measurement (Fig. S2).

2.3. Data processing

The collected EIS results were first validated via Kramer-Kronig (KK) tests [1,2] using Lin-KK [43] where the residuals of real and imaginary parts were both low (<2% from 10^5 to 10^3 Hz and <1% from 10^3 to 0.01 Hz) (Fig. S3). DRT analysis was conducted via DRT tools [44] with the elimination of impedance contributions from low-frequency (<0.1 Hz) pure capacitive diffusion [15,17,21], and all the analysis parameters were kept as the default setting except for switching regularization derivative from 1st to 2nd order. The final CNLS fitting of Nyquist plot was finished through ZSimpWin software (AMETEK).

3. Results and discussion

3.1. Interfacial process identification with DRT analysis

In the EIS analysis, the interfacial kinetics of the electrode are usually interpreted as a Voigt circuit (a series of parallel RQ elements) [45], which are displayed as a set of peaks in the DRT results. Each peak is able to show the characteristics of a specific electrode process where the peak position (local maxima) marks the time constant (τ) , and the peak magnitude (area) reveals the polarization resistance (R_p) . These parameters always follow the relation, $\tau = RC = (RQ)^{1/n}$. Here, C is the capacitance of a specific interfacial process in the ideal case (n=1) while Q, the constant phase element, indicates the one in the real condition (0 < n < 1). In DRT results, n mainly determines the extent of peak broadening [17,46].

As shown in Fig. 2, there are four peaks (P₁ to P₄) in the SOCdependent DRT results of Na/NaCrO2 cells using both PC/FEC and diglyme electrolytes, indicating probably four interfacial processes existing in the given systems. Specifically, P₁ is independent of the SOC of the cells for both PC/FEC and diglyme electrolyte systems, and its time constant remains $\sim 1.7 \times 10^{-5}$ s all the time. On the contrary, the behaviors of P2 are quite different in the two electrolytes. Upon the increase in the SOC from 10 to 100%, P2 in PC/FEC system decreases dramatically in magnitude with a small change in time constant from \sim 5 × 10⁻⁴ to \sim 3.5 × 10⁻⁴ s, whereas P₂ in diglyme system decreases slightly in magnitude as well as in the time constant from $\sim 1.9 \times 10^{-4}$ to 1.3×10^{-4} s. As for P₃ and P₄, their evolution trends in magnitude and time constant are highly similar in two electrolytes. P3 is more like a parasitic peak of P4, which is most pronounced at 10% SOC and rapidly disappears as the SOC reaches 40%. P4 keeps decreasing in the magnitude and time constant along the whole charging process.

According to our design, the electrolyte-dependent interfacial kinetics at the Na metal anodes should be the distinguishable process while the NaCrO₂ cathodes behave similarly. Since the charge-discharge curves of Na/NaCrO2 cells in the selected electrolytes are fairly close (Fig. S4), the variations captured in EIS analysis here should come from the Na metal side. Then, P2 could originate from the charge transfer process at the Na-electrolyte interface where the behaviors of this process are usually influenced by the (de)solvation and, largely, the ion diffusion in the SEI layer [20,33,47]. This identification could be further verified by the characteristic Na depositions in the two electrolytes reported by previous work [29,30,35,37]. A brief schematic of the characteristic Na deposition is presented in Fig. 1b. In PC/FEC electrolyte with the presence of an organic-rich and thick SEI layer, the initial charge transfer resistance is large. The newly deposited Na tends to form dendritic and porous structures accompanied with locally increased surface area and attenuated SEI layer. This leads to more Na-ion diffusion paths with shortened diffusion length, which definitely lowers the difficulty in the charge transfer at the Na metal side over the charging

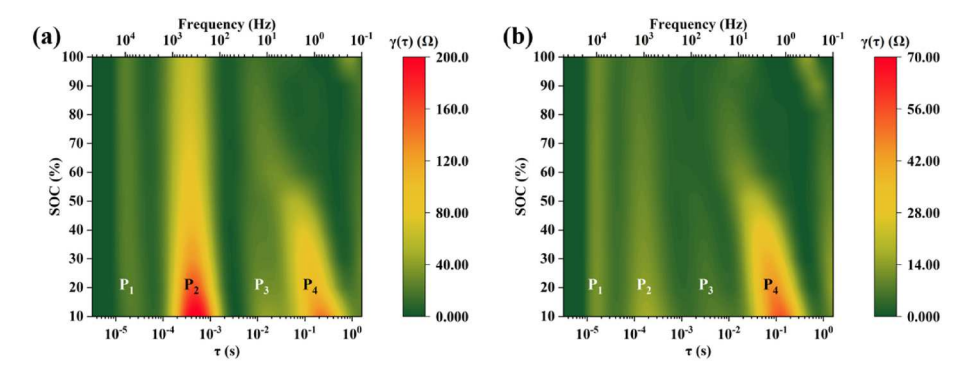


Fig. 2. SOC-dependent DRT results of Na/NaCrO₂ cells with (a) PC/FEC and (b) diglyme electrolytes. 2D DRT plots are used in this work to display the peak evolution trend over the variation of testing conditions in a more evident manner.

process. At the same time, both increased surface area and attenuated SEI layer thickness should result in an increase in capacitance for this process. This matches well the relation, $\tau=RC=(RQ)^{1/n}$, since a significant decrease in resistance does not lead to a similar evolution in time constant, indicating the corresponding capacitance is growing here. As for diglyme system, the present SEI layer is inorganic-rich and thin, making it easier for Na ions to hop through. Thus, the initial charge transfer resistance is small. Due to the relatively flat and dense Na deposition, the charge transfer resistance as well as the corresponding time constant only decrease mildly in the charging process. Therefore, P_2 is attributed to the (de)sovlation and the Na-ion diffusion in the SEI layer.

Regarding P1, showing up at such a low time constant (a high frequency) and being neither SOC nor electrolyte dependent, it probably stems from the contact between electrode components and current collector [16,17,20,26,41]. As for P_3 and P_4 , it is apparent that they are both closely related to the charge transfer at the cathode side. Without the presence of the CEI layer due to the lack of electrolyte oxidation at the given upper cutoff (3.6 V) [36,48], the process behavior is determined by (de)solvation and, mainly, Na-ion concentrations inside the cathode particles. At the early stage of charging process, Na-ion deintercalation at the cathode-electrolyte interface is hindered by the lack of Na-ion vacancies in NaCrO2 particles, leading to a large charge transfer resistance. As charging continues, Na ions are continuously extracted from NaCrO2 particles, leaving more and more vacant sites in the layered structures. Thereby, the charge transfer resistance should keep decreasing at the cathode side. Besides, the NaCrO2 particle surface is generally invariant within one cycle, implying little change in the corresponding capacitance. All of these expected physical features at the cathode side perfectly match the evolution behaviors of P4, and are widely applied in the EIS analysis for the Li analogues too [20,24,41,49]. Provided with the relation, $\tau = RC = (RQ)^{1/n}$, the capacitance of this process is assumed to be rather stable since both peak magnitude and time constant decrease at the same time. Hence, P4 is taken as a major charge transfer process at the cathode-electrolyte interface here. Considering the ambiguous characteristics of P3, such as weak in magnitude and valid only at the low SOC, it is regarded as an incomplete (de)solvation process, a minor charge transfer process. Possibly, owing to the sluggish faradaic reactions at the low SOC, the overall charge transfer process at the cathode surface may separate into a few elementary steps, like P3 and P4 in this case, which could be distinguished via different time constants in the DRT analysis. As the cell charging continues, P₃ gradually merges with the major charge transfer process because of the lowered resistance in the faradaic reactions as we just mentioned. Thus, P3, with a minor contribution to the total polarization, could also arise from the charge transfer at the cathode side.

The peak identification discussed above is further confirmed through temperature-dependent DRT results of Na/NaCrO $_2$ at 10% SOC (Fig. 3). Clearly, as the testing temperature increases from 0 to 40 $^{\circ}$ C, the number of interfacial kinetics remains four regardless of the electrolyte systems,

which is identical with what is observed in the SOC-dependent DRT results. P1, beside its independency of electrolytes and SOC, is almost independent of temperature as well. This is compatible with our previous judgement that it comes from the contact resistance between electrode components and the current collector. The peak characteristics of P₂ here are also consistent with the surface conditions of the Na metal anode in the given electrolytes. The presence of a much thicker SEI layer in PC/FEC electrolyte severely hinders the relevant Na-ion diffusion process compared to that in diglyme electrolyte, leading to a much pronounced temperature dependency. With respect to P3 and P4, both of them are temperature dependent and their charge transfer resistances decrease as temperature increases. Moreover, it seems that, except for P₁, the other interfacial processes always have smaller time constants in diglyme electrolyte than in PC/FEC electrolyte no matter for SOCdependent or temperature-dependent EIS measurements, indicating a comprehensively faster kinetic in diglyme electrolyte than in PC/FEC electrolyte for Na/NaCrO2 system. Similar findings are reported previously in other NIB systems too [30,33,38]. Based on the analysis towards DRT results, the existing interfacial processes and corresponding DRT peaks are summarized in Table 1.

3.2. Nyquist plot interpretation with DRT-assisted ECM

Through identifying the existing interfacial kinetics with DRT analysis, an ECM with rational physical meanings for Na/NaCrO $_2$ cells is proposed in Fig. 4. $R_{\rm e}$ represents ohmic resistance of the bulk electronic and ionic conduction. $R_{\rm c,cont.}Q_{\rm c,cont.}$, $R_{\rm a,sei}Q_{\rm a,sei}$, and $R_{\rm c,ct}Q_{\rm c,ct}$ elements stand for the previously resolved losses from electrode/current collector contact, ion diffusion in the SEI, and charge transfer at the cathode surface, respectively. W, Warburg element, comes from the solid diffusion happening at low-frequency domain. As shown in Figs. 6 and 7, Nyquist plots from SOC- and temperature-dependent EIS measurements are fitted well with the proposed ECM, respectively. In this popular impedance format, understanding the evolution of impedance contributions from each electrode processes becomes more familiar. To facilitate such interpretation, different interfacial kinetics are labeled with specific color in Figs. 5 and 6.

Table 1 Summary of identified DRT peaks, physical origins, and corresponding frequency regions (25 $^{\circ}$ C).

DRT peak names	Physical origins	Frequency regions (Hz)	Identified peak names
P_1	Contact resistance between electrode components and current collector.	$\begin{array}{l} \sim\!2\times10^4 \text{ to} \\ \sim\!3\times10^3 \end{array}$	P _{c,cont}
P_2	(De)solvation and Na-ion diffusion in the SEI layer.	$\begin{array}{l} \sim \! 3 \times 10^3 \text{ to} \\ \sim \! 4 \times 10^1 \end{array}$	$P_{a,sei}$
P ₃ and P ₄	Charge transfer at cathode- electrolyte interface.	$\sim 10^2 \text{ to } \sim 10^{-1}$	$P_{c,ct}$

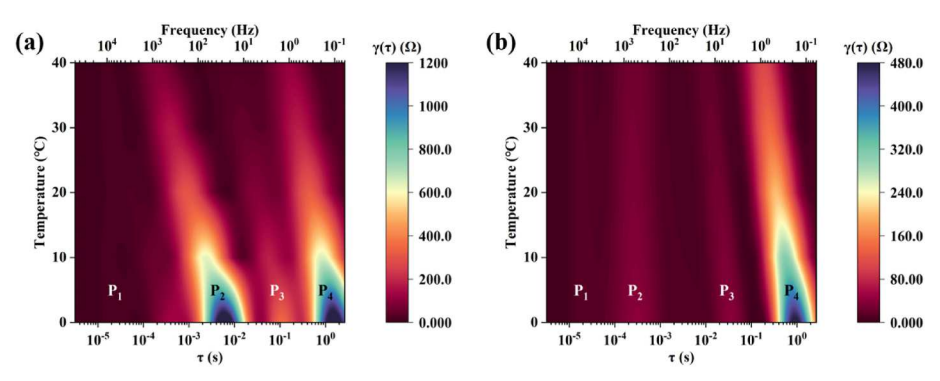


Fig. 3. Temperature-dependent DRT results of Na/NaCrO2 cells at 10% SOC in (a) PC/FEC and (b) diglyme electrolytes.

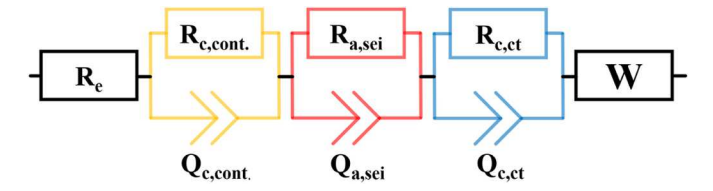


Fig. 4. ECM established based on DRT analysis.

Basically, the overall cell impedance of PC/FEC system is always higher than that of diglyme system. During the charging process at room temperature, the cell kinetic is affected by both cathode and anode

processes with PC/FEC electrolyte while it is dominated by the cathode charge transfer process with diglyme electrolyte. In terms of the temperature-dependent Nyquist plots, the whole charge transfer kinetic is extremely sluggish in PC/FEC system, especially when the testing temperature goes down to 0 $^{\circ}$ C. These electrolyte-dependent features will be later related to the corresponding activation energies through the Arrhenius equation.

3.3. Performance-limiting process confirmation with activation energies

The Arrhenius relationships and activation energies of the related electrode processes are summarized in Fig. 7. Given the Arrhenius equation associated with polarization resistance [20]:

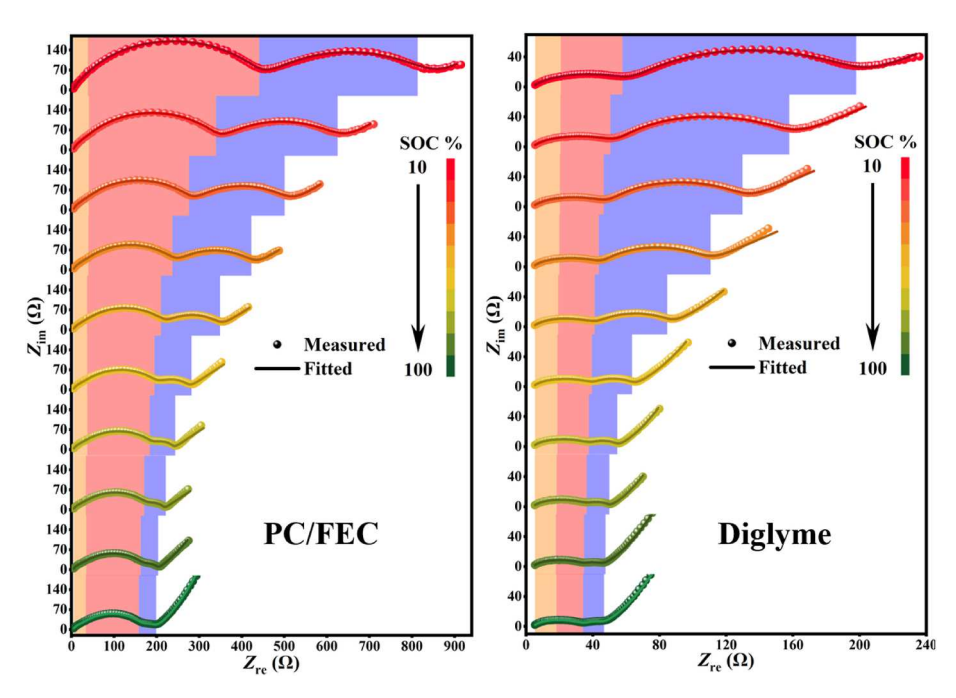


Fig. 5. Primary and fitted Nyquist plots from SOC-dependent EIS measurements for Na/NaCrO2 cells with PC/FEC and diglyme electrolytes.

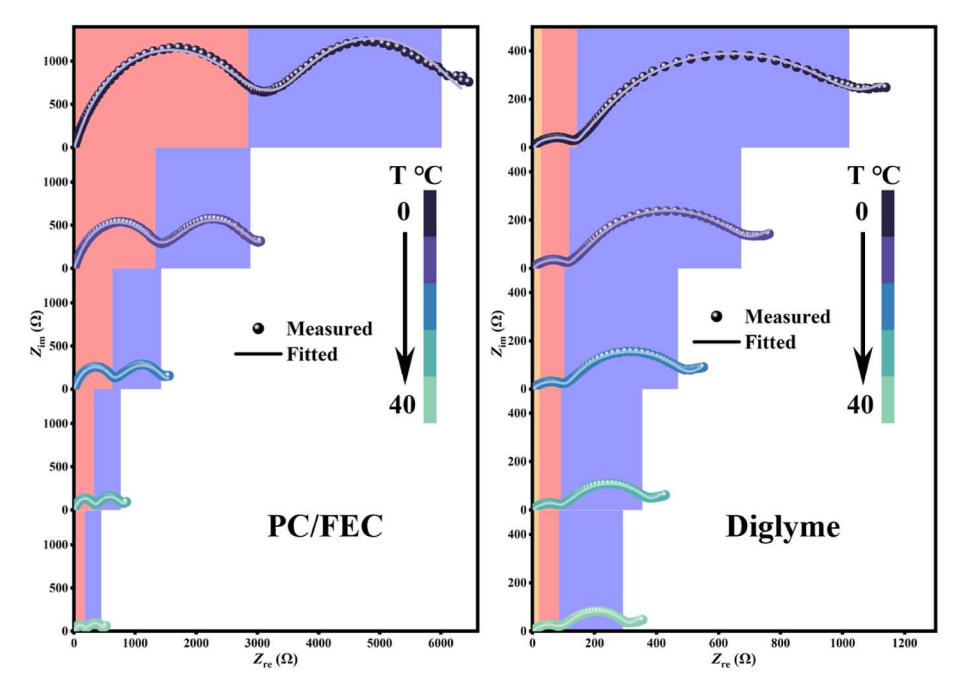


Fig. 6. Primary and fitted Nyquist plots from temperature-dependent EIS measurements for Na/NaCrO2 cells with PC/FEC and diglyme electrolytes.

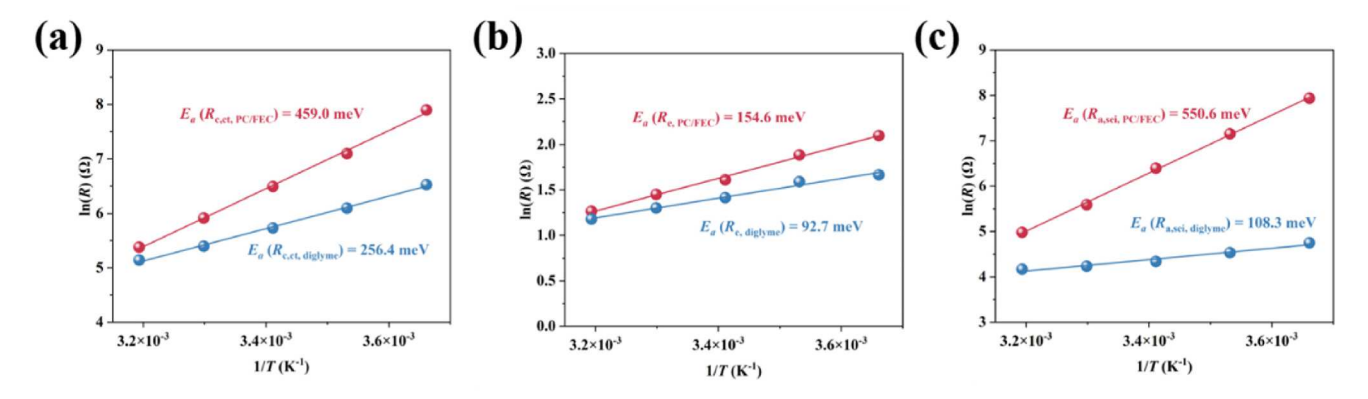


Fig. 7. Activation energies of (a) the charge transfer process at the NaCrO₂ cathode side, (b) the ionic conduction in the electrolyte, and (c) the charge transfer process at the Na metal anode side in the selected electrolytes.

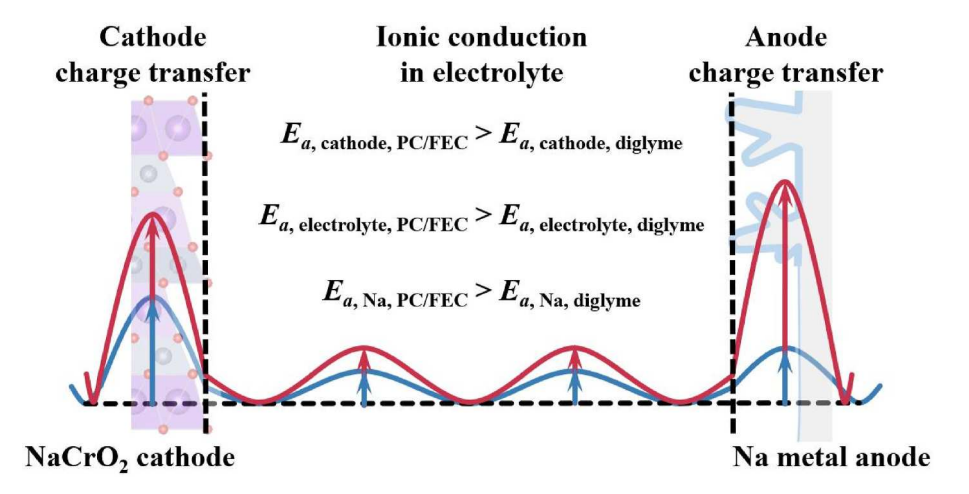


Fig. 8. A schematic demonstrating the relative activation energies as well as the performance-limiting processes for Na/NaCrO₂ cells with PC/FEC (\bullet) and diglyme electrolyte (\bullet).

$$\frac{1}{R} = Ae^{-\frac{E_a}{k_B T}} \tag{1}$$

where R is the polarization resistance of a specific electrode process; A is a proportionality constant; E_a is the activation energy required to trigger certain kinetic; k_B is Boltzmann constant; T is the testing temperature. Thereby, a linear relation between ln(R) and 1/T could be obtained where the slope of the fitted curve is the activation energy, E_a .

It is clear from Fig. 7 that both NaCrO₂ cathode and Na metal anode have relatively faster kinetics in the diglyme electrolyte than in the PC/ FEC one. The activation energy of Re (Fig. 7b) is closely relevant to the ionic conduction in the electrolyte. The lower E_a and R_e for diglyme electrolyte could be caused by the smaller solvent viscosity where ionic conduction is facilitated via faster mass transfer [50]. As for the charge transfer at the cathode side (Fig. 7a), the E_a for PC/FEC system is almost twice the one for diglyme system, which could originate from the (de) solvation process. Since the cell SOC is fixed at 10% for the temperature-dependent EIS measurements, the (de)intercalation of Na ions in NaCrO2 crystals should be similar for both systems. Thus, the cause of this variation is probably from difference in the salt-solvent (NaPF₆ towards PC/FEC or diglyme) interactions in the electrolyte. Per previous studies on such electrolytes, the DFT calculated solvation energy of Na⁺-PC complex is much higher than that of Na⁺-diglyme one [38], which is consistent with the results acquired through EIS study of this work. With regard to the charge transfer at the Na metal side, the energy barrier in PC/FEC electrolyte is four times higher than that in diglyme one. Likely, this tardy interfacial process is the result of both the slow (de)solvation and the hindered Na-ion diffusion in the organic-rich thick SEI layer.

Furthermore, the cell kinetics could be reflected on the chargedischarge profile as well. As shown in Figs. S4 and S5, it is obvious that lower overpotentials are present with the diglyme electrolyte, regardless of the oxidation or reduction of the NaCrO2 working electrode. This implies that when Na metal is used as the counter electrode, the electrochemical characteristics could be altered with the inappropriate selection of electrolyte system. Specifically, this work shows that NaCrO₂ cells can underperform with the PC/FEC electrolyte due to the undesirable counter electrode (Na metal) kinetics. Therefore, although most novel electrode materials for NIBs are first evaluated in conventional ester-based electrolytes [11,13,39,42], proper ester-based electrolytes should be used as the standard electrolytes to validate the electrochemical performance of the emerging electrode materials in a more accurate manner. In this way, the performance-limiting origins discovered in the Na metal cells will be closer to the real causes other than the illusions created by the failure of the Na metal counter electrode.

4. Conclusions

In this work, the EIS results of a NIB system, $Na/NaCrO_2$, are successfully deconvoluted via applying DRT analysis and electrolyte-dependent Na metal labeling, which separates the cell impedance into five parts, including bulk electrolyte resistance, contact impedance from electrode-current collector interface, polarization from Na-ion (de)

solvation and SEI-diffusion on the Na metal surface, charge transfer impedance from Na-ion (de)solvation and faradaic reaction at the $\rm NaCrO_2$ cathode, and low-frequency solid state Warburg diffusion. This demonstrates a novel logic in interpreting the EIS results of NIB studies, and provides an ECM with reasonable physical motivations, which could be implemented to fit Nyquist plots from NIBs in the future.

The performance-limiting steps of Na/NaCrO₂ system in PC/FEC and diglyme electrolytes are disclosed by comparing the activation energies of corresponding electrode processes. As displayed in Fig. 8, it is noted that the electrochemical performance is mainly determined by the working electrode itself in the cell with diglyme electrolyte, while it is affected by both the working and Na metal counter electrode in the cell with PC/FEC electrolyte. Accordingly, appropriate ether-based electrolytes, like diglyme, should be used instead of traditional ester-based ones, like PC/FEC, to describe the precise electrochemical activity of emerging electrode materials for NIBs. Hopefully, the work of this study could benefit the application of EIS and the evaluation of standard electrolytes in other battery chemistry as well.

CRediT authorship contribution statement

Changlong Chen: Conceptualization, Methodology, Data curation, Formal analysis, Writing – original draft, preparation, All authors have read and agreed to the published version of the manuscript. Hao Lin: Methodology, Data curation, Formal analysis, All authors have read and agreed to the published version of the manuscript. Bingyu Liu: Data curation, All authors have read and agreed to the published version of the manuscript. Leon Shaw: Methodology, Formal analysis, Writing – review & editing, Supervision, Project administration, Funding acquisition, All authors have read and agreed to the published version of the manuscript.

Declaration of competing interest

The authors of the manuscript titled "Deconvolution of the Electrochemical Impedance of $Na/NaCrO_2$ Cells with Ester- and Ether-Based Electrolytes" declare no conflict of interest.

Data availability

Data will be made available on request.

Appendix A. Supplementary data

Supplementary data to this article can be found online at https://doi.org/10.1016/j.jpowsour.2023.233465.

References

- [1] S. Wang, J. Zhang, O. Gharbi, V. Vivier, M. Gao, M.E. Orazem, Nat. Rev. Dis. Prim. 1 (2021).
- [2] V. Vivier, M.E. Orazem, Chem. Rev. 122 (2022) 11131–11168.
- [3] Q. He, M. Ashuri, Y. Liu, B. Liu, L. Shaw, ACS Appl. Energy Mater. 4 (2021) 4744–4757.
- [4] A.R.C. Bredar, A.L. Chown, A.R. Burton, B.H. Farnum, ACS Appl. Energy Mater. 3 (2020) 66–98.
- [5] V.J. Gelling, M.M. Wiest, D.E. Tallman, G.P. Bierwagen, G.G. Wallace, Prog. Org. Coating 43 (2001) 149–157.
- [6] D.D. Macdonald, Electrochim. Acta 56 (2011) 1761–1772.

- [7] N. Meddings, M. Heinrich, F. Overney, J.S. Lee, V. Ruiz, E. Napolitano, S. Seitz, G. Hinds, R. Raccichini, M. Gabers, J. Park, J. Power Sources 480 (2020).
- [8] M. Gaberscek, Nat. Commun. 12 (2021) 6513.
- [9] N. Yabuuchi, K. Kubota, M. Dahbi, S. Komaba, Chem. Rev. 114 (2014) 11636–11682.
- [10] Nat. Energy 7 (2022) 461, 461.
- [11] Y. Wang, W. Li, G. Hu, Z. Peng, Y. Cao, H. Gao, K. Du, J.B. Goodenough, Chem. Mater. 31 (2019) 5214–5223.
- [12] J. Chen, Y. Peng, Y. Yin, Z. Fang, Y. Cao, Y. Wang, X. Dong, Y. Xia, Angew. Chem., Int. Ed. Engl. 60 (2021) 23858–23862.
- [13] X.G. Yuan, Y.J. Guo, L. Gan, X.A. Yang, W.H. He, X.S. Zhang, Y.X. Yin, S. Xin, H. R. Yao, Z.G. Huang, Y.G. Guo, Adv. Funct. Mater. 32 (2022).
- [14] Z. Lu, C. Geng, H. Yang, P. He, S. Wu, Q.H. Yang, H. Zhou, Proc. Natl. Acad. Sci. USA 119 (2022), e2210203119.
- [15] M. Luo, A.L. Ortiz, L. Shaw, J. Electrochem. Soc. 166 (2019) A3546–A3553.
- [16] J.P. Schmidt, T. Chrobak, M. Ender, J. Illig, D. Klotz, E. Ivers-Tiffee, J. Power Sources 196 (2011) 5342–5348.
- [17] J. Illig, M. Ender, T. Chrobak, J.P. Schmidt, D. Klotz, E. Ivers-Tiffee, J. Electrochem. Soc. 159 (2012) A952–A960.
- [18] R. Petibon, C.P. Aiken, N.N. Sinha, J.C. Burns, H. Ye, C.M. VanElzen, G. Jain, S. Trussler, J.R. Dahn, J. Electrochem. Soc. 160 (2012) A117–A124.
- [19] T. Momma, T. Yokoshima, H. Nara, Y. Gima, T. Osaka, Electrochim. Acta 131 (2014) 195–201.
- [20] A.S. Keefe, S. Buteau, I.G. Hill, J.R. Dahn, J. Electrochem. Soc. 166 (2019) A3272–A3279.
- [21] K. Pan, F. Zou, M. Canova, Y. Zhu, J.H. Kim, J. Power Sources 479 (2020).
- [22] M. Steinhauer, S. Risse, N. Wagner, K.A. Friedrich, Electrochim. Acta 228 (2017) 652–658.
- [23] D.E. Brown, E.J. McShane, Z.M. Konz, K.B. Knudsen, B.D. McCloskey, Cell Rep. Phys. Sci. 2 (2021).
- [24] X. Chen, L.Y. Li, M.M. Liu, T. Huang, A.S. Yu, J. Power Sources 496 (2021).
- [25] P. Gargh, A. Sarkar, Y.H. Lui, S. Shen, C. Hu, S. Hu, I.C. Nlebedim, P. Shrotriya, J. Power Sources 485 (2021).
- [26] M. Gaberscek, J. Moskon, B. Erjavec, R. Dominko, J. Jamnik, Electrochem. Solid State Lett. 11 (2008) A170–A174.
- [27] X. Zhou, J. Huang, Z.Q. Pan, M.G. Ouyang, J. Power Sources 426 (2019) 216–222.
- [28] B. Lee, E. Paek, D. Mitlin, S.W. Lee, Chem. Rev. 119 (2019) 5416–5460.
- [29] R. Rodriguez, K.E. Loeffler, S.S. Nathan, J.K. Sheavly, A. Dolocan, A. Heller, C. B. Mullins, ACS Energy Lett. 2 (2017) 2051–2057.
- [30] B. Ma, Y. Lee, P. Bai, Adv. Sci. 8 (2021), 2005006.
- [31] Y. Jin, P.M.L. Le, P.Y. Gao, Y.B. Xu, B.W. Xiao, M.H. Engelhard, X. Cao, T.D. Vo, J. T. Hu, L.R. Zhong, B.E. Matthews, R. Yi, C.M. Wang, X.L. Li, J. Liu, J.G. Zhang, Nat. Energy 7 (2022) 718–725.
- [32] B. Han, Y. Zou, Z. Zhang, X. Yang, X. Shi, H. Meng, H. Wang, K. Xu, Y. Deng, M. Gu, Nat. Commun. 12 (2021) 3066.
- [33] K. Li, J. Zhang, D. Lin, D.W. Wang, B. Li, W. Lv, S. Sun, Y.B. He, F. Kang, Q.H. Yang, L. Zhou, T.Y. Zhang, Nat. Commun. 10 (2019) 725.
- [34] A. Hofmann, Z.Q. Wang, S.P. Bautista, M. Weil, F. Muller, R. Lowe, L. Schneider, I. Ul Mohsin, T. Hanemann, Electrochim. Acta 403 (2022).
- [35] X. Zheng, S. Weng, W. Luo, B. Chen, X. Zhang, Z. Gu, H. Wang, X. Ye, X. Liu, L. Huang, X. Wu, X. Wang, Y. Huang, Research 2022 (2022), 9754612.
- [36] R. Mogensen, S. Colbin, R. Younesi, Batteries Supercaps 4 (2021) 791–814.
- [37] Z.W. Seh, J. Sun, Y. Sun, Y. Cui, ACS Cent. Sci. 1 (2015) 449-455.
- [38] Y.C. Zhen, R.J. Sa, K.Q. Zhou, L.Y. Ding, Y. Chen, S. Mathur, Z.S. Hong, Nano Energy 74 (2020).
- [39] M. Luo, A.L. Ortiz, L. Shaw, ACS Appl. Energy Mater. 3 (2020) 7216–7227.
- [40] K. Kubota, I. Ikeuchi, T. Nakayama, C. Takei, N. Yabuuchi, H. Shiiba, M. Nakayama, S. Komaba, J. Phys. Chem. C 119 (2014) 166–175.
- [41] Y. Lu, C.Z. Zhao, J.Q. Huang, Q. Zhang, Joule 6 (2022) 1172–1198.
- [42] M. Sawicki, A. Ortiz, M. Luo, L. Shaw, Chemelectrochem 4 (2017) 3222-3230.
- [43] M. Schönleber, D. Klotz, E. Ivers-Tiffée, Electrochim. Acta 131 (2014) 20–27.
- [44] T.H. Wan, M. Saccoccio, C. Chen, F. Ciucci, Electrochim. Acta 184 (2015) 483–499.
 [45] S. Buteau, D.C. Dahn, J.R. Dahn, J. Electrochem. Soc. 165 (2018) A228–A234.
- [45] S. Buteatt, D.C. Dann, J.R. Dann, J. Electrochem. Soc. 165 (2018) A228–A234.
 [46] A. Leonide, V. Sonn, A. Weber, E. Ivers-Tiffee, J. Electrochem. Soc. 155 (2008) B36–B41.
- [47] T.R. Jow, S.A. Delp, J.L. Allen, J.P. Jones, M.C. Smart, J. Electrochem. Soc. 165 (2018) A361–A367.
- [48] K. Westman, R. Dugas, P. Jankowski, W. Wieczorek, G. Gachot, M. Morcrette, E. Irisarri, A. Ponrouch, M.R. Palacin, J.M. Tarascon, P. Johansson, ACS Appl. Energy Mater. 1 (2018) 2671–2680.
- [49] P. Shafiei Sabet, G. Stahl, D.U. Sauer, J. Power Sources 472 (2020).
- [50] Z. Tian, Y. Zou, G. Liu, Y. Wang, J. Yin, J. Ming, H.N. Alshareef, Adv. Sci. 9 (2022), e2201207.